Electronic Supplementary Information for

Dealloying-driven nanoporous palladium with superior electrochemical actuation performance

Jie Zhang, Qingguo Bai, Zhonghua Zhang*

Key Laboratory for Liquid-Solid Structural Evolution and Processing of Materials (Ministry of Education), School of Materials Science and Engineering, Shandong University, Jingshi Road 17923, Jinan, 250061, P.R. China

*Corresponding author. Email: zh_zhang@sdu.edu.cn (Z. Zhang)

This part includes:

Figs. S1- S19

Tables S1-S2

(a)

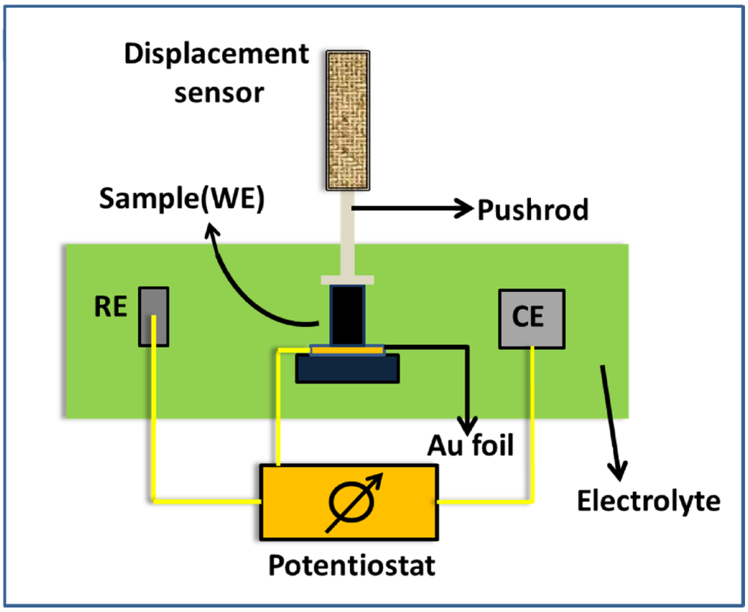
Displacement sensor
Sample(WE)
Pushrod
RE
CE
Au foil
Electrolyte
Potentiostat

(b)

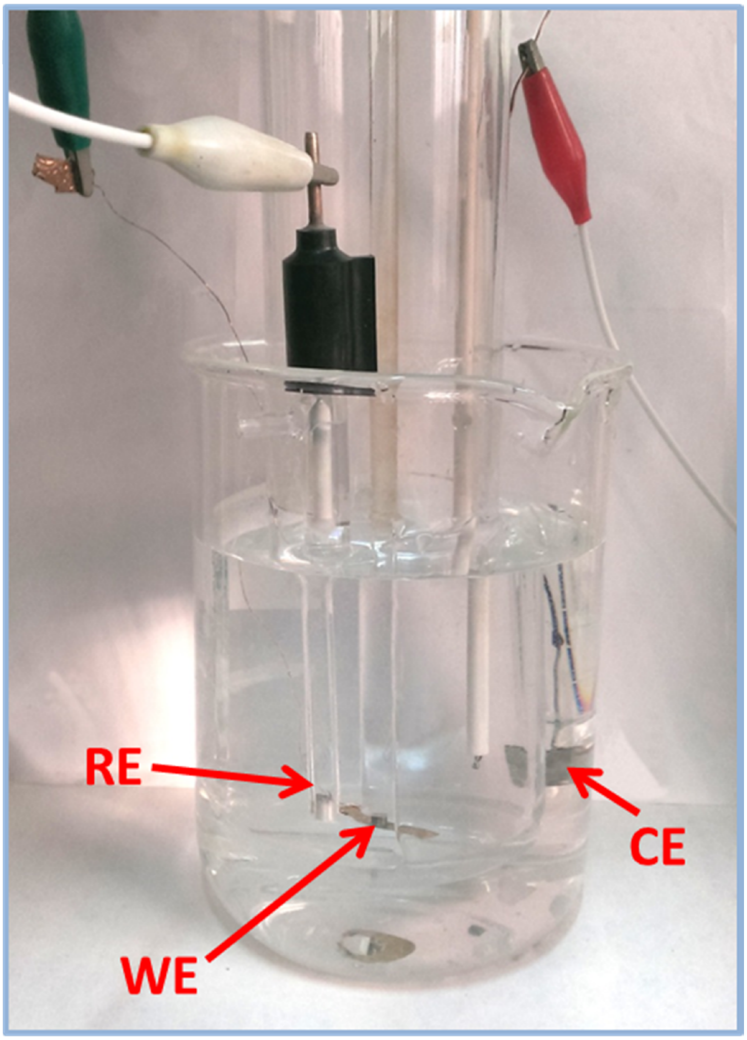
RE
CE
WE

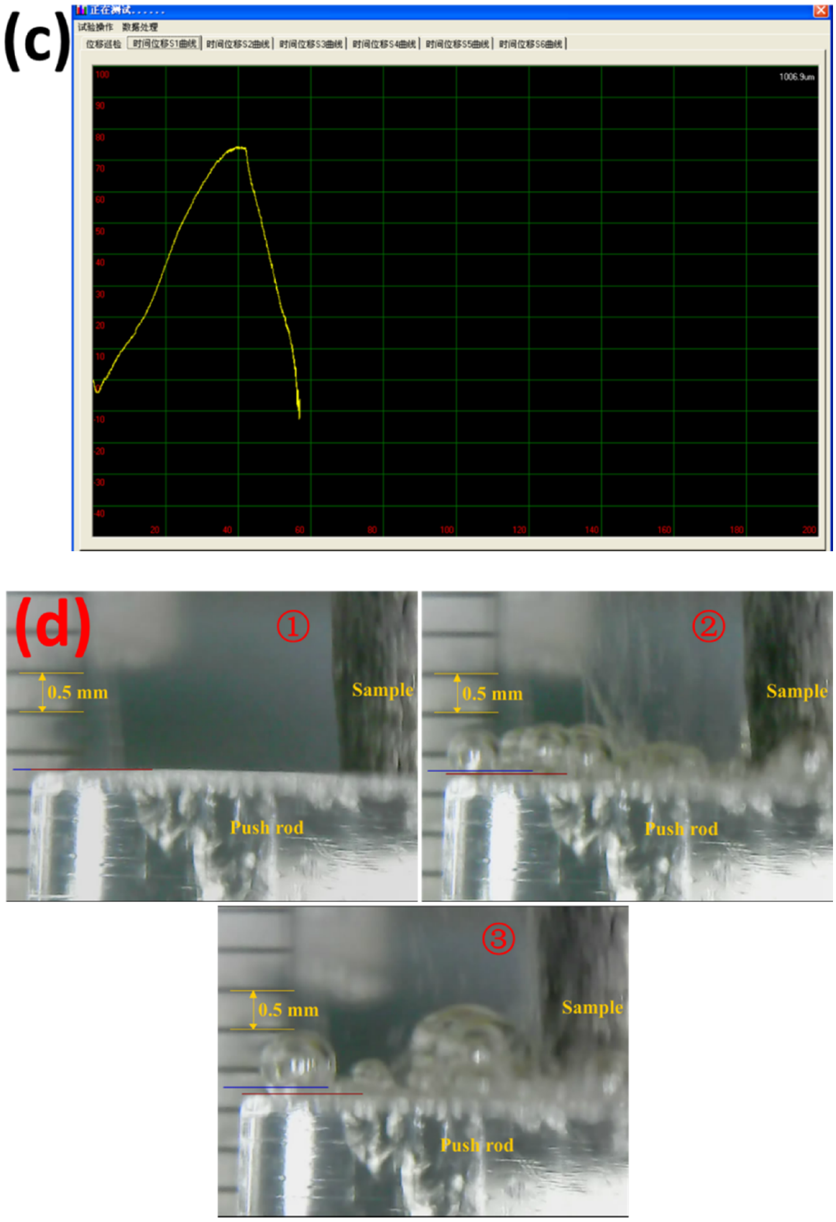

Figure S1. (a)Schematic illustration of the measuring apparatus for electrochemical actuation (CE: counter electrode, RE: reference electrode). The bulk np-Pd rod was directly used as the working electrode (WE). (b) Photograph of the electrochemical cell which was connected with the potentiostat and the displacement sensor. (c) Image of data-recording window for the in situ dilatometry experiment (length change, μm) of sample 2 (L_0 = 2.6 mm). (d) Selected optical images for the in situ dilatometry experiment process, showing the expansion of the np-Pd rod which drove the movement of the push rod (from the position marked by the blue line to another position highlighted by the brown line). One can also see the supporting video clip in the ESI.

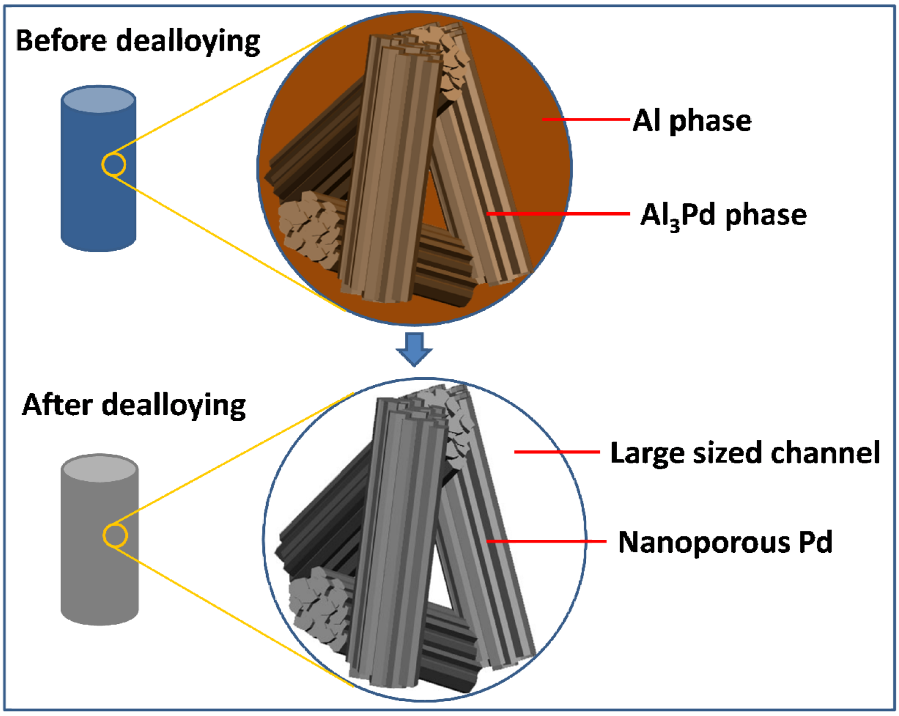

Figure S2. Schematic illustration showing the dealloying strategy for fabrication of bulk np-Pd rods. Before dealloying, the Al-Pd precursor alloy has a hybrid-phase structure composed of bicontinuous interpenetrating Al and Al_3Pd phases (top part of the figure). Moreover, the Al_3Pd phase is comprised of parallel bars forming clusters in the longitudinal direction. During dealloying, the less noble Al phase is preferentially etched away leaving large-sized channels which allow rapid penetration of the dealloying solution into the interior of the bulk precursor. At the same time, the more noble Al_3Pd phase undergoes the dealloying, resulting in the formation of nanoporous structure (bottom part of the figure). Furthermore, the cluster-like morphology of Al_3Pd phase could be retained into the as-dealloyed samples. Through this dealloying strategy, we could fabricate bulk np-Pd with a hierarchically porous structure.

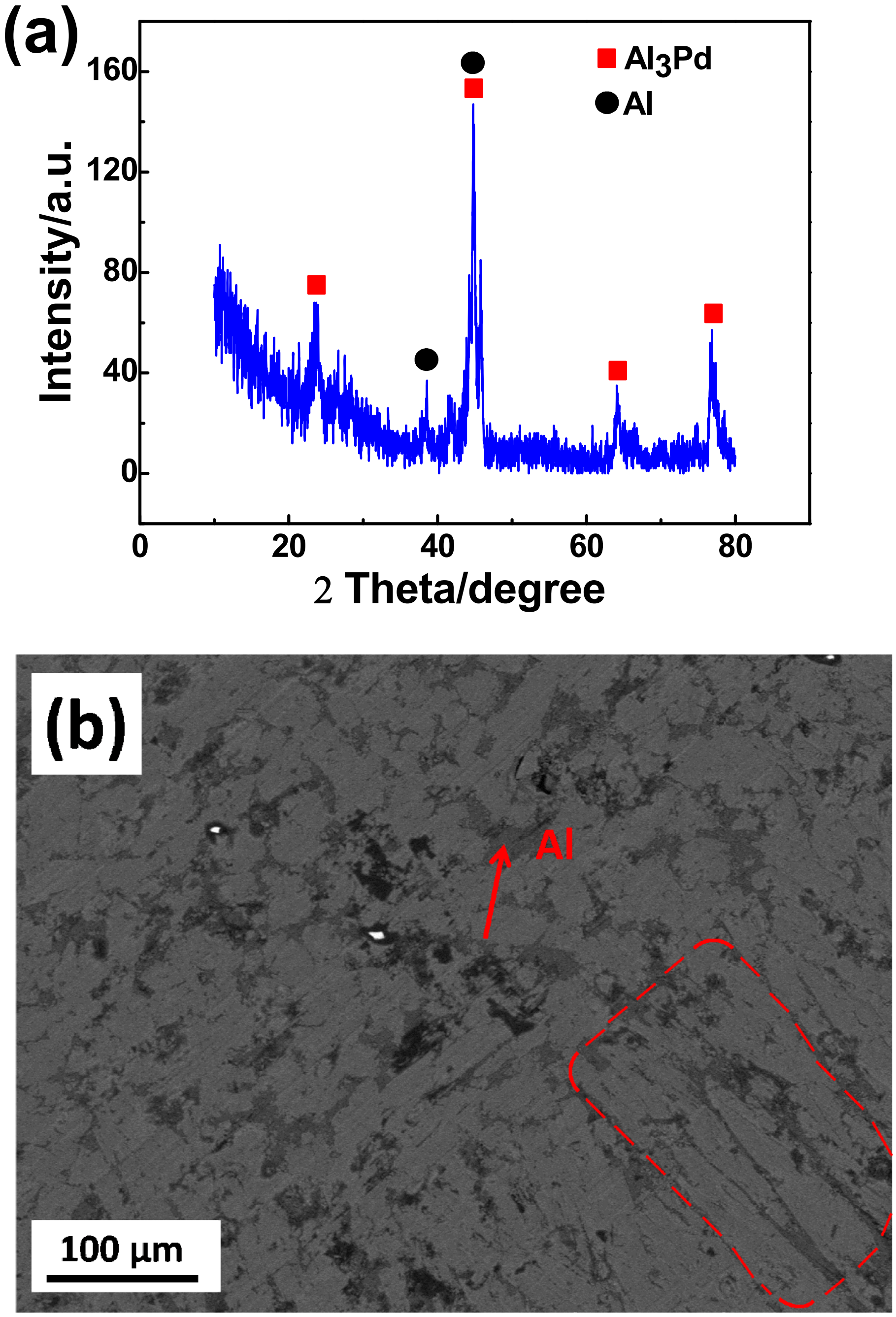

Figure S3. Structural characterization of the $Al_{80}Pd_{20}$ precursor alloy. (a) X-ray diffraction (XRD) pattern confirming that the $Al_{80}Pd_{20}$ precursor is composed of Al and Al_3Pd phases. (b) Back-scattered electron (BSE) image of the cross-section of the $Al_{80}Pd_{20}$ rod after 20 s of immersion in a 0.5 wt.% HF solution. The dark grey areas are the Al phase (one area is highlighted by a red arrow) while the light grey areas are the Al_3Pd phase. Both the two phases interpenetrate with each other. Moreover, the bar-cluster structure of Al_3Pd can be clearly observed, as marked by a dashed rectangle in Figure S3b. The microstructure of the $Al_{80}Pd_{20}$ precursor is consistent with the alloy design in Figure S2.

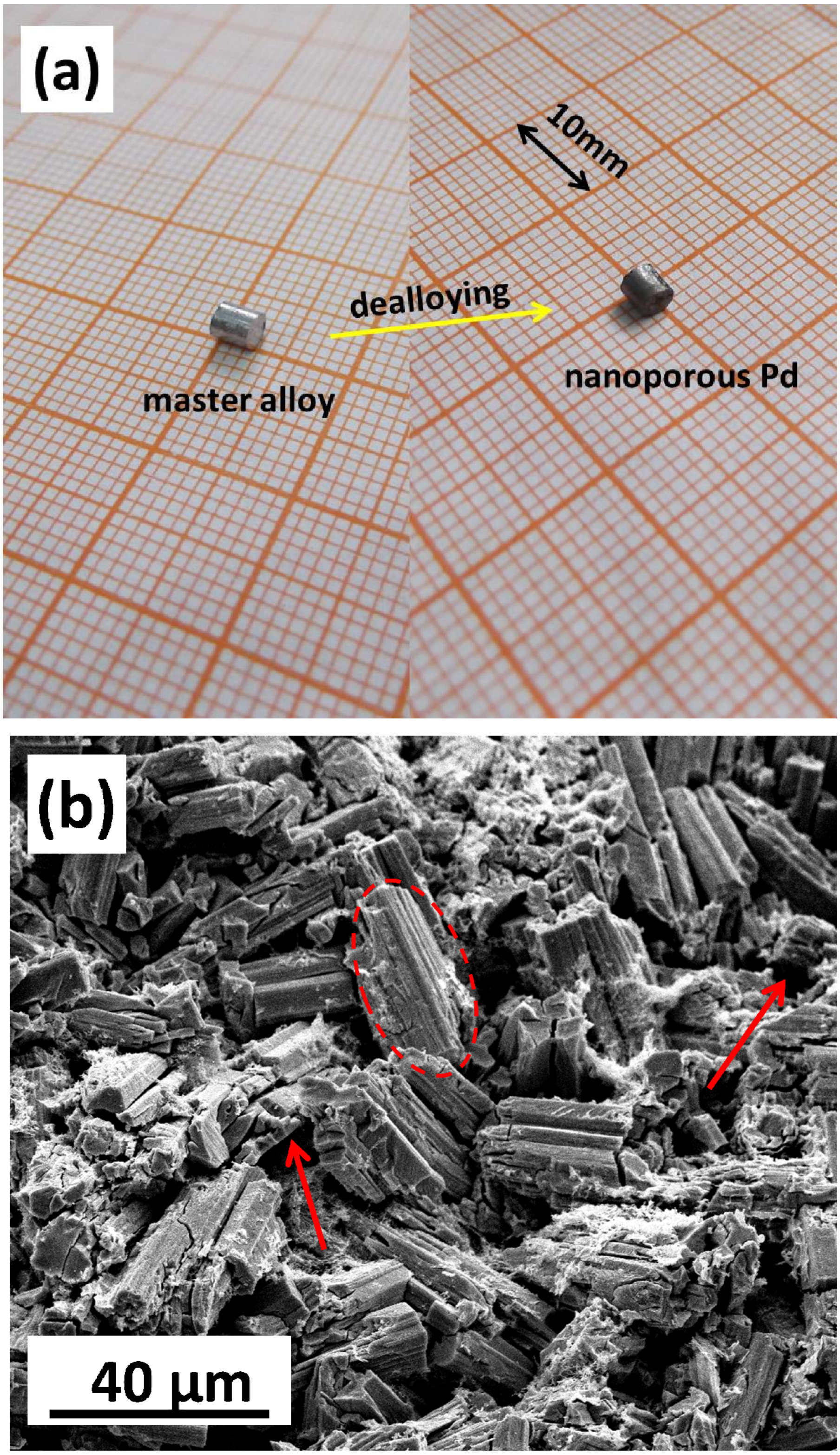

Figure S4. (a) Macrographs of the $Al_{80}Pd_{20}$ precursor rod (left) and the bulk np-Pd rod (right). (b) Section-view SEM image of the bulk np-Pd rod. The bulk np-Pd rod is mainly composed of randomly distributed clusters comprised of parallel bars (one cluster is marked by a dashed ellipse), and the large-sized channels can be clearly observed (as highlighted by red arrows). The clusters originate from the Al_3Pd phase and the large sized channels come from the Al phase. The microstructure of the bulk np-Pd rod is in good agreement with that proposed in Figure S2.

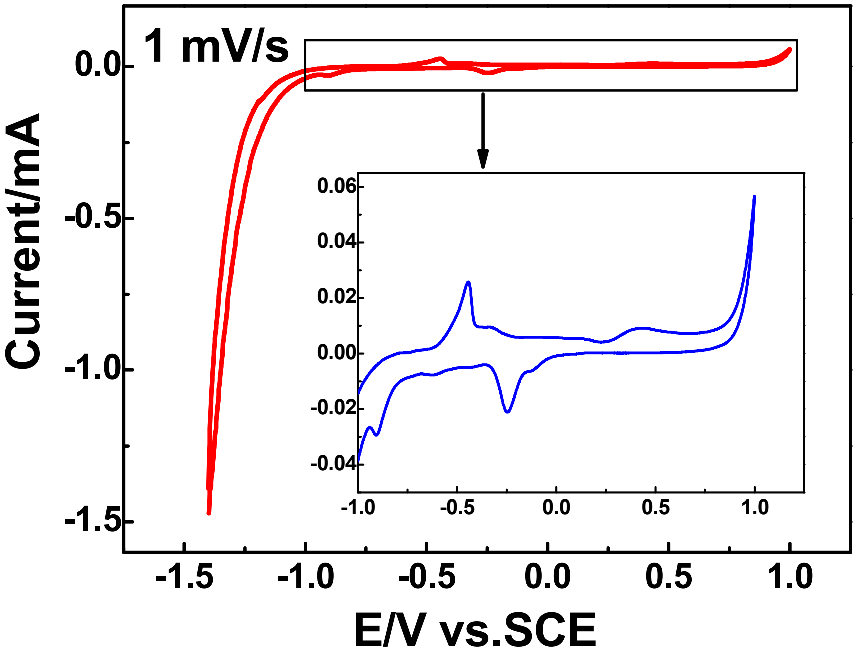

Figure S5. CV curve of nanostructured Pd powders in the 0.7 M NaF aqueous solution at the scan rate of 1 mV/s. The electrode was prepared as follows. 1.26 mg nanostructured Pd with the particle size of less than 10 nm, 5.04 mg XC-72 carbon powder, 1.5 mL isopropanol and 0.5 mL Nafion solution (0.5 wt.%) were ultrasonically mixed for 30 min. Afterwards, 8 μL slurry was dropped on a freshly polished glassy carbon (GC) electrode with a diameter of 4 mm. Before CV measurement, the coated GC electrode was dried in a vacuum tank at room temperature for at least 3 h.

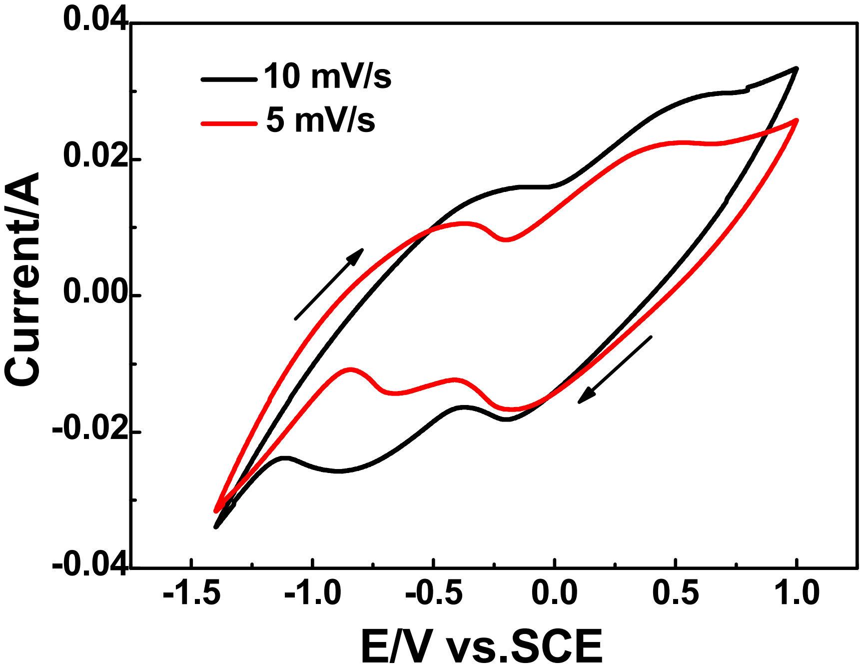

Figure S6. CV curves of the bulk np-Pd rod in the 0.7 M NaF aqueous solution at different scan rates.

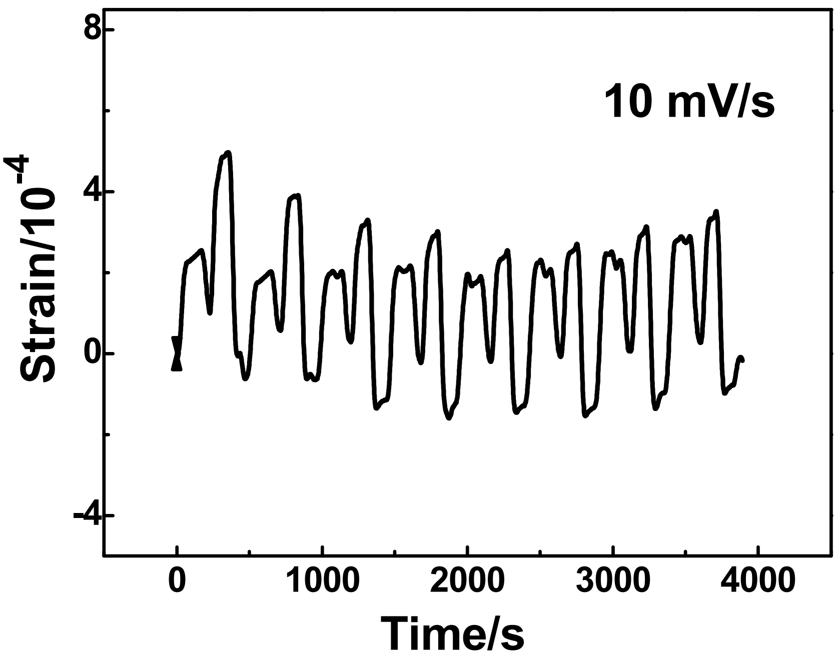

Figure S7. CV induced reversible strain of the bulk np-Pd rod in the 0.7 M NaF aqueous solution at the scan rate of 10 mV/s. Here, successive eight cycles are presented.

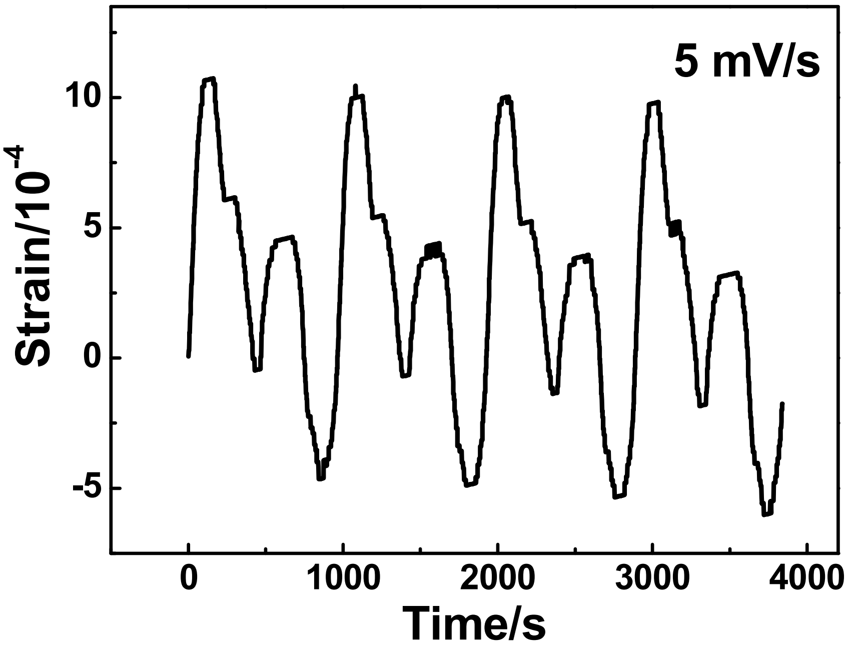

Figure S8. CV induced reversible strain of the bulk np-Pd rod in the 0.7 M NaF aqueous solution at the scan rate of 5 mV/s. Here, successive four cycles are presented.

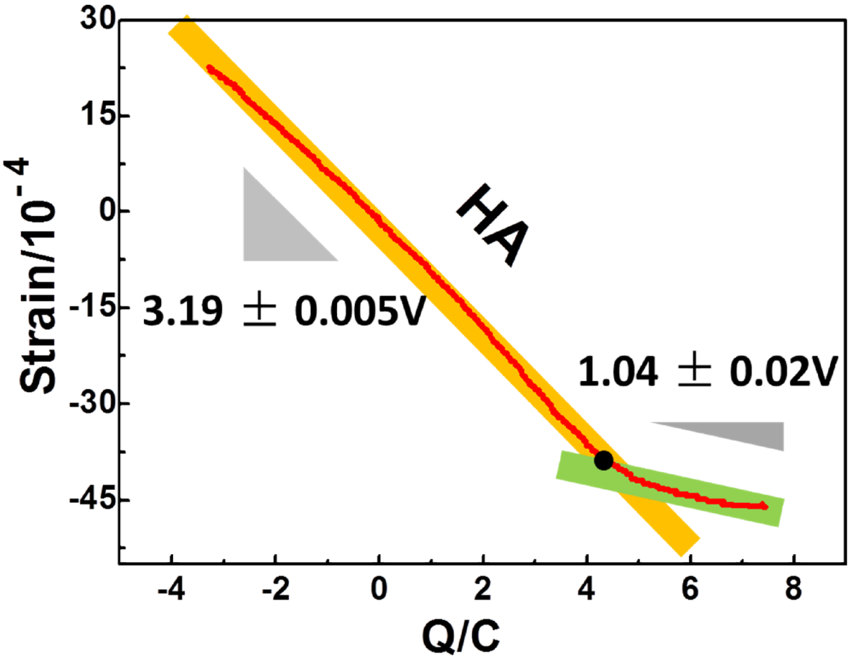

Figure S9. Reversible strain (red curve) of the bulk np-Pd versus the transferred (net) charge Q at the scan rate of 1 mV/s in the hydrogen adsorption-absorption (HA) region. Two-stage linear correlations with different slopes could be clearly observed, implying distinct hydrogen adsorption/absorption behaviors of the present bulk np-Pd. The associated stress-charge coefficients are also presented beside the curve.

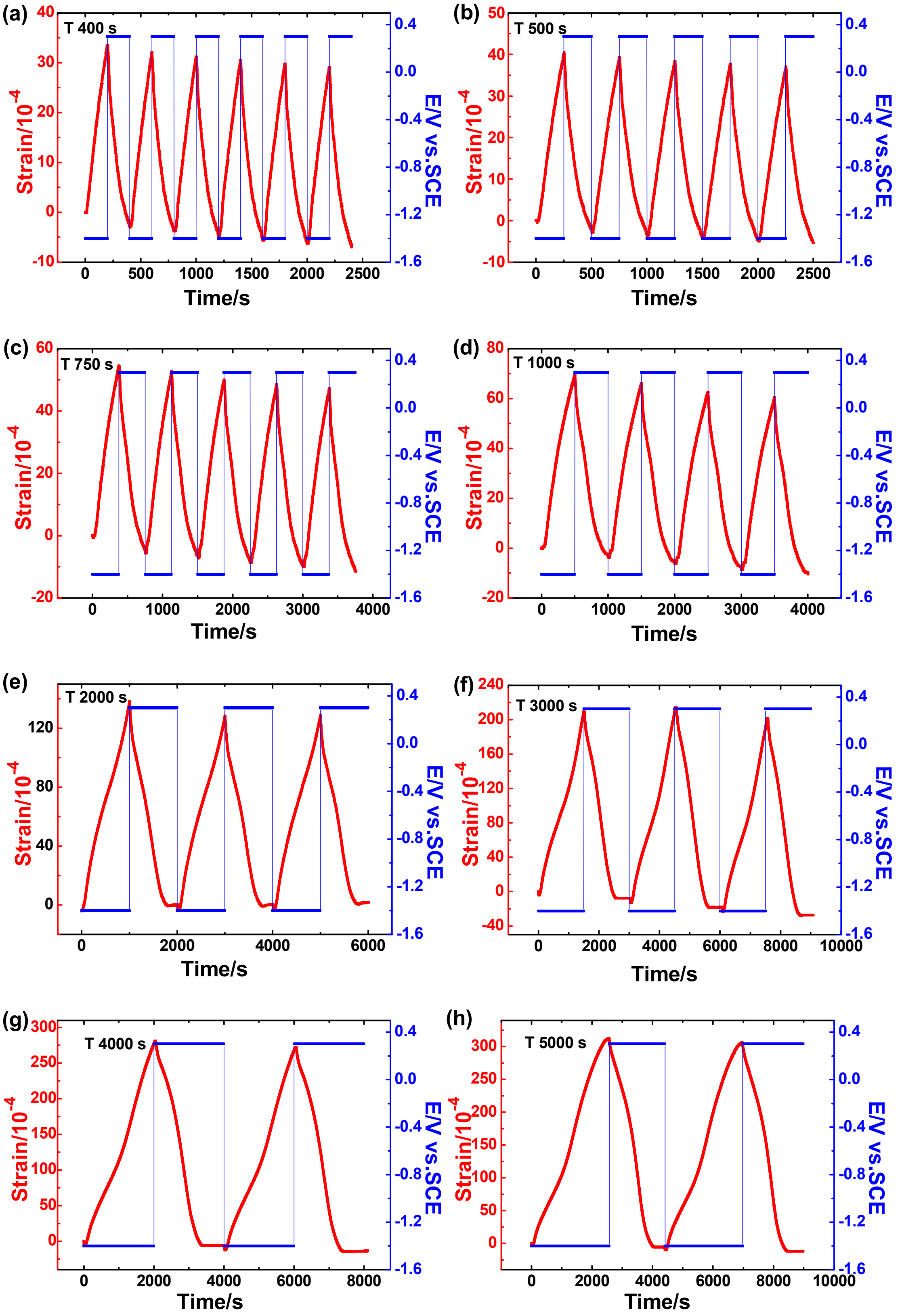

Figure S10. The SWP induced reversible strain of the bulk np-Pd in the 0.7 M NaF aqueous solution at different periods. The applied potential was periodically switched between -1.4 and +0.3 V vs. SCE, and the bulk np-Pd accordingly expanded and contracted.

Table S1. The related parameters of the bulk np-Pd at different periods.

Period(s)	**Maximum strain rate (10^{-5} s^{-1}) Expansion/contraction**	**Stress- charge coefficient (V)**	**Maximum reversible strain (10^{-4})**	**Maximum transferred charge (C)**
200	2.6/3.5	2.6 ± 0.04	18.8	-2.6
400	2.3/3.6	2.5 ± 0.02	34.4	-5.1
500	2.1/3.7	2.6 ± 0.02	41.4	-6.6
750	2.0/3.5	2.6 ± 0.01	58.4	-9.5
1000	2.0/3.9	2.5 ± 0.01	68.6	-12.2
2000	2.1/3.9	2.6 ± 0.01	125.8	-22
3000	2.1/3.1	/	227.4	-31.6
4000	2.0/3.0	/	284.9	-38.7
5000	2.0/3.0	/	315.8	-45
5500	1.8/2.9	/	328.1	-47.7

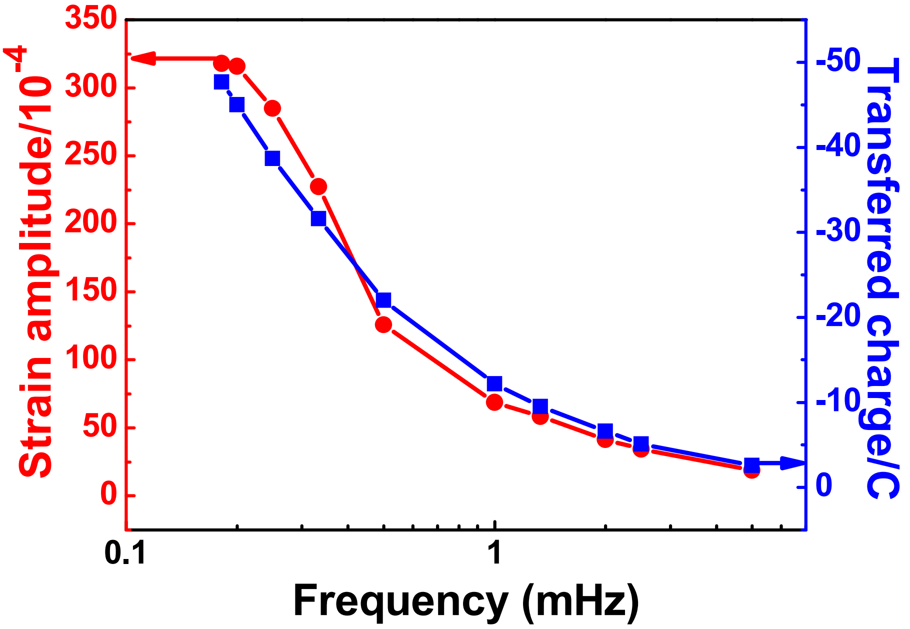

Figure S11. The SWP-induced strain amplitude of the bulk np-Pd and the involved maximum transferred charge versus the frequency (the reciprocal of the period). The data were obtained from Figure 3 and Figure S10.

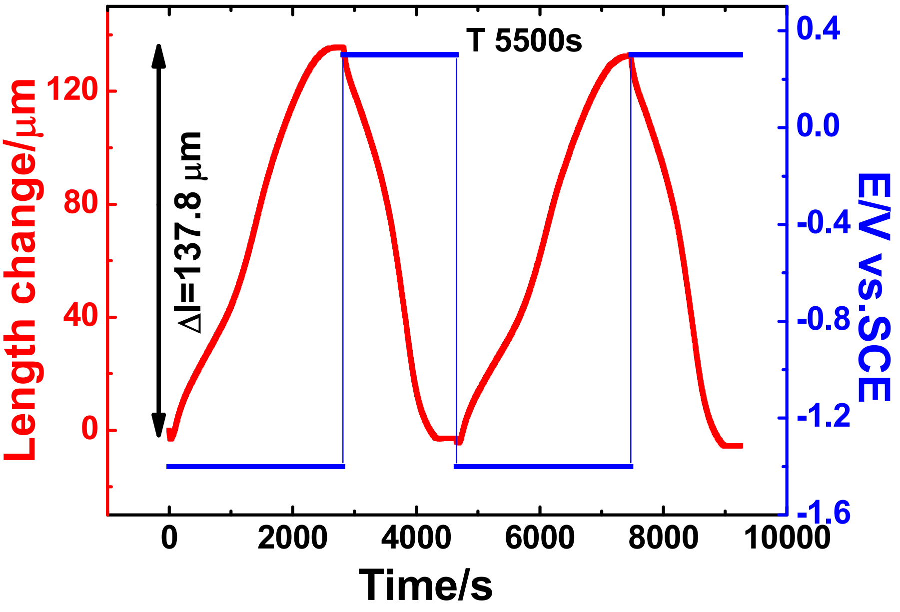

Figure S12. The SWP-induced reversible length change ΔL of the bulk np-Pd rod versus time at the period of 5500 s. The maximum strain stroke reaches up to 137.8 μm for the np-Pd rod with the initial length of 4.2 mm.

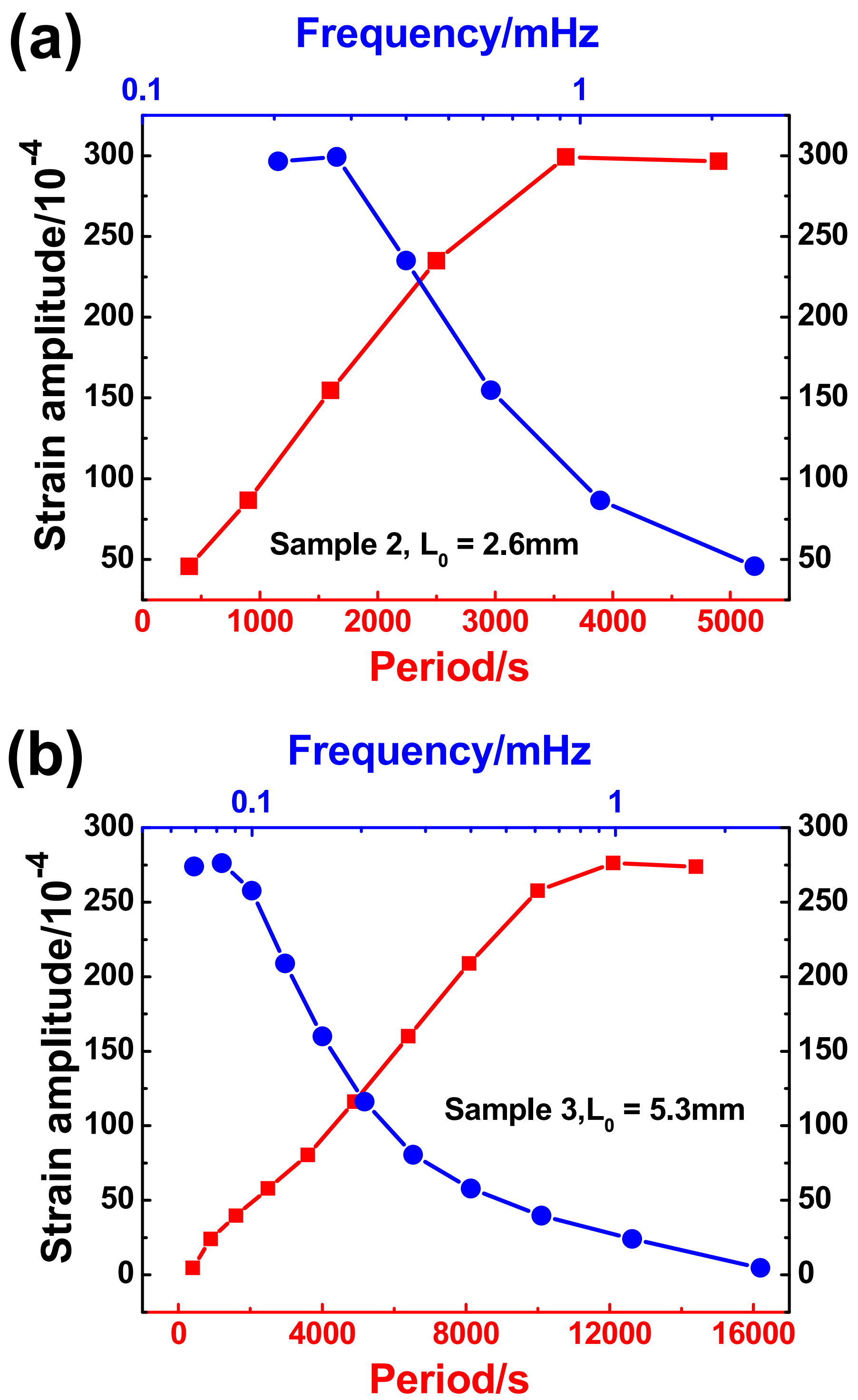

Figure S13. The SWP-induced reversible strain amplitude of the bulk np-Pd rods with the length of (a) 2.6 mm and (b) 5.3 mm versus the period (bottom coordinate) as well as the corresponding frequency (top coordinate). The electrolyte is the 0.7 M NaF aqueous solution.

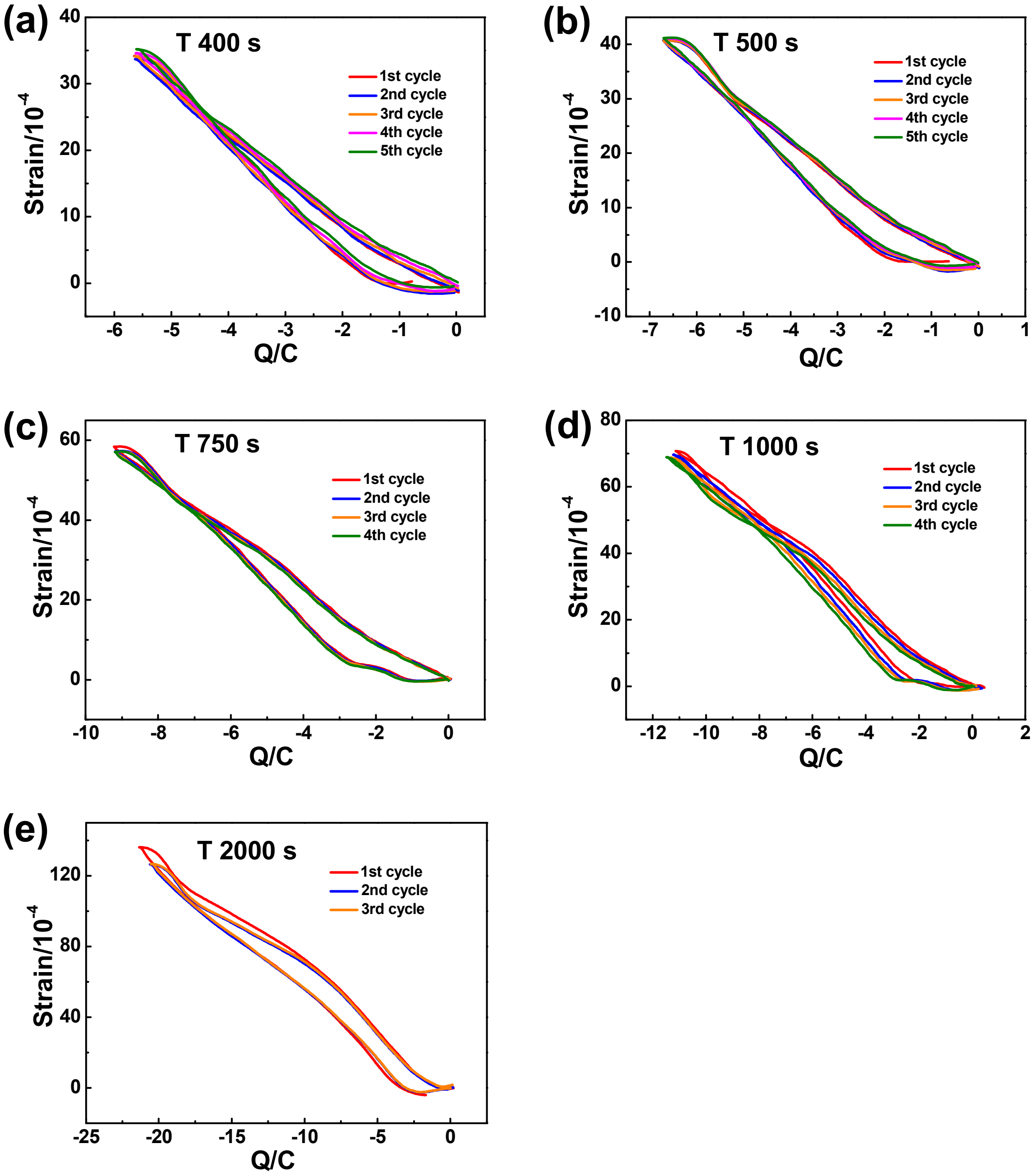

Figure S14. The SWP-induced reversible strain of the bulk np-Pd rod versus the transferred charge at different periods.

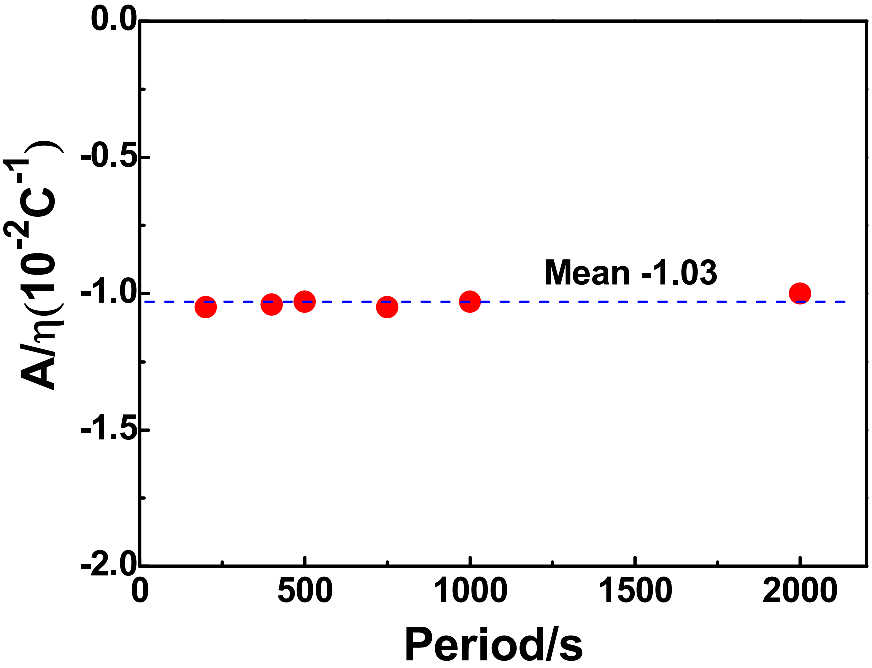

Figure S15. The A/η values as a function of the period. Here *x* is the fraction of H in Pd (H-to-Pd atomic ratio, PdH_x).

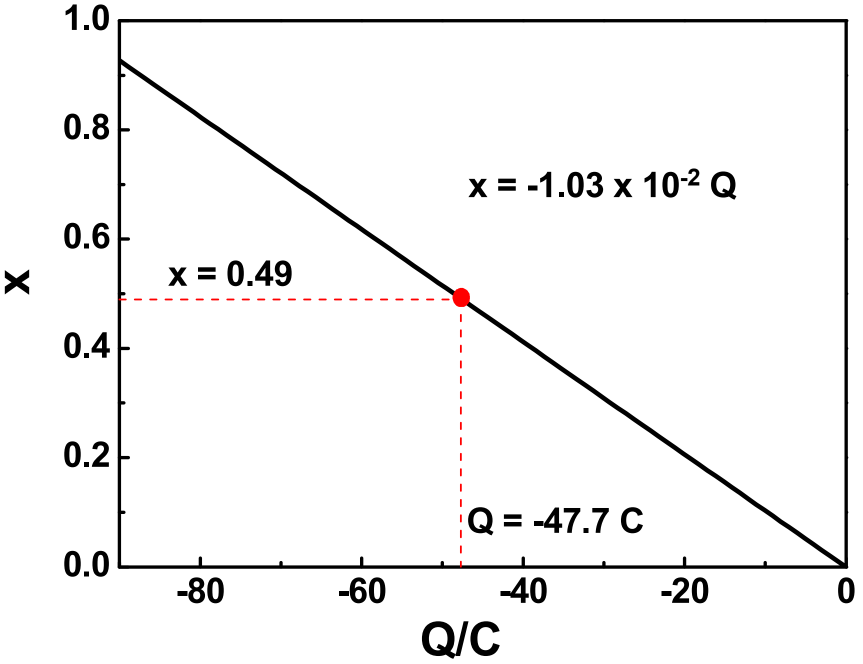

Figure S16. The absorbed H fraction (x in PdH_x) as a function of the involved transferred charge (Q). For the SWP period of T = 5500 s (Figure 3b), the overall transferred charge is – 47.7 C and the corresponding x value is around 0.49 ($PdH_{0.49}$).

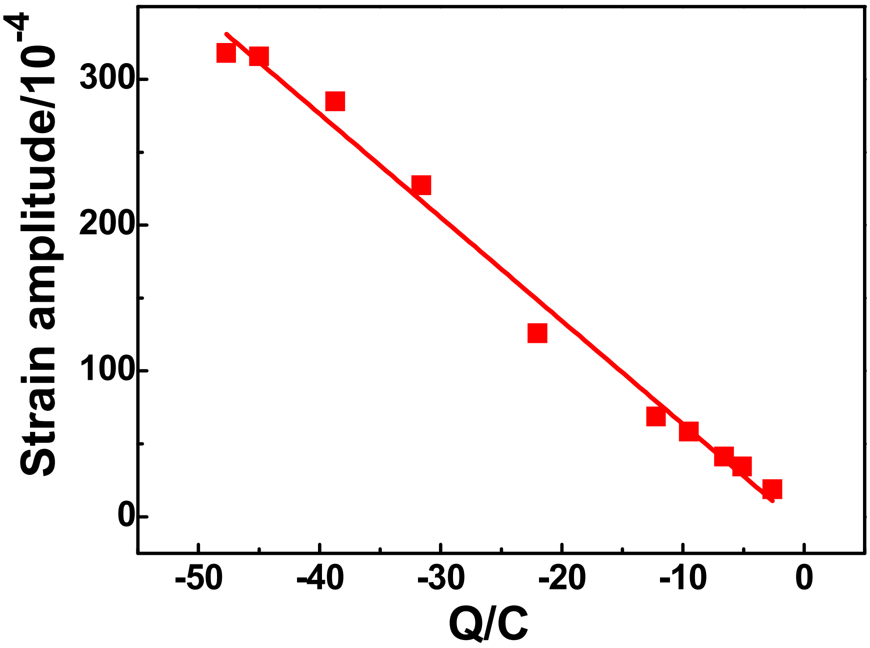

Figure S17. The SWP-induced strain amplitude of the bulk np-Pd rod versus the overall transferred charge. It can be seen that the strain amplitude of np-Pd linearly increases with the increase of the overall transferred charge (here, absolute value).

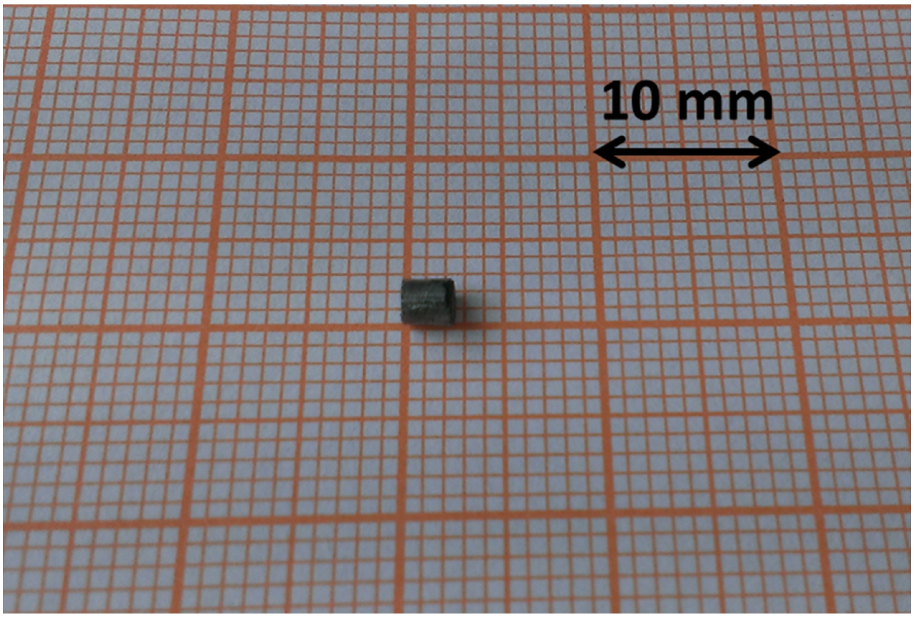

Figure S18. Photograph of one np-Pd rod after the electrochemical actuation measurements.

Table S2. Figures of merit for various actuator materials.

Materials	**Y(GPa)**	**$\varepsilon_{\max}$(10^{-4})**	**w_v(MJ m^{-3})**	**w_M(J kg^{-1})**	**U/V**
skeletal muscle[1]	0.01- 0.06	>4000	0.04	40	/
Piezoceramic[2]	64	20	0.13	4.25	100
electrostrictor polymer[2]	1.1	450	1.1	500	10000
dielectric elastomer(VHB)[3]	0.001-0.003	>30000	3.4	/	1000
carbon nanotube actuator[4,5]	640	50	8	/	~2
nanoporous carbon[6]	0.28	220	/	81	2
np palladium (our work)	**6.63**	**328**	**10.71**	**3811**	**~2**

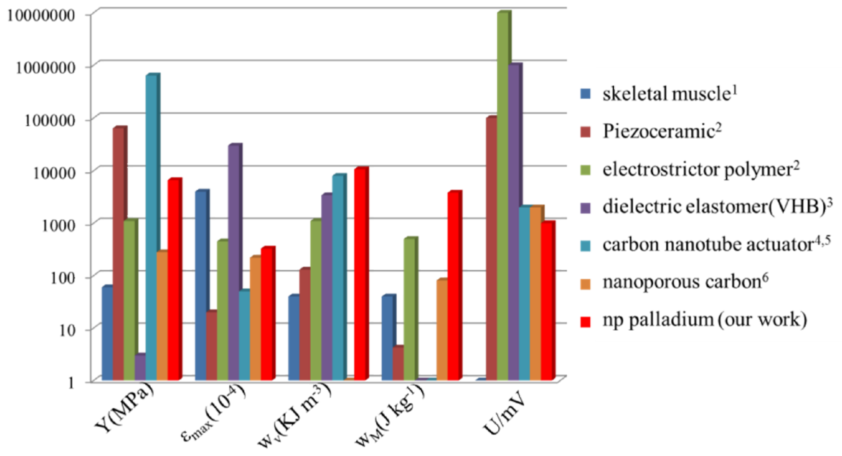

Figure S19. Column chart plot of characteristics of various actuator materials. Y: Young's modulus, ε_{max}: maximum strain amplitude, w_V: volume-specific strain energy density, w_M: mass-specific strain energy density, U: operating voltage.

1 J. D. W. Madden, N. A. Vandesteeg, P. A. Anquetil, P. G. A. Madden, A. Takshi, R. Z. Pytel, S. R. Lafontaine, P. A. Wieringa, I. W. Hunter, *IEEE J. Oceanic Eng.* 2004, **29**, 706-728.

2 Q. M. Zhang, V. Bharti, X. Zhao, *Science* 1998, **280**, 2101-2104.

3 R. Pelrine, R. Kornbluh, Q. Pei, J. Joseph, *Science* 2000, **287**, 836-839.

4 R. H. Baughman, *Science* 1999, **284**, 1340-1344.

5 M. Hughes, G. M. Spinks, *Adv. Mater.* 2005, **17**, 443-446.

6 L.-H. Shao, J. Biener, H.-J. Jin, M. M. Biener, T. F. Baumann, J. Weissmueller, *Adv. Funct. Mater.* 2012, **22**, 3029-3034.